

Article

Safety and Reliability Analysis of Reconfigurable Battery Energy Storage System

Helin Xu, Lin Cheng *, Daniyaer Paizulamu and Haoyu Zheng 

Department of Electrical Engineering, Tsinghua University, Beijing 100084, China; xuhl20@mails.tsinghua.edu.cn (H.X.); dnyepzlm22@mails.tsinghua.edu.cn (D.P.); zhenghy24@mails.tsinghua.edu.cn (H.Z.)

* Correspondence: chenglin@mail.tsinghua.edu.cn

Abstract: Lithium-ion batteries (LIBs) are widely used in electric vehicles (EVs) and energy storage systems (ESSs) because of their high energy density, low self-discharge rate, good cycling performance, and environmental friendliness. Nevertheless, with the extensive utilization of LIBs, incidents of fires and explosions resulting from thermal runaway (TR) have become increasingly prevalent. The resolution of safety concerns associated with LIBs and the reduction in operational risks have become pivotal to the operation and control of ESSs. This paper proposes a model for the TR process of LIBs. By simplifying the modeling of TR reactions, it is possible to calculate the starting temperature of the battery self-heating reaction. Subsequently, this paper puts forth an operational reliability evaluation algorithm for a reconfigurable battery energy storage system (BESS). Finally, this paper develops a control algorithm for reliability improvement, with the objective of ensuring safe and stable control of the ESS.

Keywords: lithium-ion battery; reconfigurable topology; thermal runaway; control strategy

1. Introduction



Academic Editor: Vilas Pol

Received: 1 November 2024

Revised: 24 December 2024

Accepted: 28 December 2024

Published: 30 December 2024

Citation: Xu, H.; Cheng, L.; Paizulamu, D.; Zheng, H. Safety and Reliability Analysis of Reconfigurable Battery Energy Storage System. *Batteries* **2025**, *11*, 12. <https://doi.org/10.3390/batteries11010012>

Copyright: © 2024 by the authors. Licensee MDPI, Basel, Switzerland. This article is an open access article distributed under the terms and conditions of the Creative Commons Attribution (CC BY) license (<https://creativecommons.org/licenses/by/4.0/>).

The substantial consumption and utilization of fossil fuels, including oil and natural gas, has resulted in two significant challenges confronting humanity in the 21st century: environmental contamination and an impending energy crisis. In light of the mounting environmental crises, China put forth a proposal at the 75th United Nations General Assembly, declaring its intention to attain a peak in carbon emissions by 2030 and to strive for carbon neutrality by 2060. The implementation of the established national policy is facilitating significant transformations within China's power industry, which is consequently evolving into a new energy industry pattern. In order to achieve the carbon reduction target, the proportion of new energy power generation represented by wind power and photovoltaics is continuing to increase. In the preceding decade, the cost of photovoltaic and wind power has decreased markedly, thereby establishing the foundation for the subsequent and rapid increase in installed capacity. By 2022, China's installed capacity for renewable energy is expected to exceed 1.5 billion KW [1]. Nevertheless, the intermittent and unstable properties of photovoltaic and wind power present a significant challenge to their integration into the power grid and meeting the demands of users. ESS is defined as the utilization of specific devices and systems for the purpose of storing energy and subsequently releasing it when required, thereby facilitating the transfer of energy in a timely and spatial manner. This represents a pivotal advance in the large-scale integration of renewable energy into the power grid. Accordingly, energy storage is regarded as a crucial component in the development of a novel power system.

A BESS facilitates the processes of energy storage, release, and management through batteries, representing one of the most widely applied and promising power storage technologies in the contemporary era. Compared to pumped hydro storage, electrochemical storage is less constrained by geographical conditions, has shorter construction periods, and can be flexibly applied across various segments of power systems and other diverse scenarios [2]. The main types of electrochemical storage include lead-acid batteries, lead-carbon batteries, LIBs, sodium-ion batteries, sodium-sulfur batteries, and flow batteries. The International Energy Agency (IEA) pointed out that LIBs dominate both EV and storage applications, demonstrated by the market share for LiFePO₄ (LFP) batteries rising to 40% of EV sales and 80% of new battery storage in 2023 [3].

Nevertheless, LIBs continue to present certain safety concerns. On occasion, incidents of fire, deflagration, and even explosions occur in EVs and energy storage power stations, both domestically and abroad. The primary cause of such incidents is TR. From a macro perspective, during the operation of LIBs, when the heat generated inside the lithium battery is higher than the heat dissipation, the temperature of the LIB itself will rise with the increase in operating time. Upon reaching the critical temperature for TR, the heat generation within the battery will continue to increase due to the occurrence of side reactions. This will eventually result in the decomposition of active substances, leading to a significant rise in temperature and, ultimately, fire [4]. Statistics from the Electric Power Research Institute of the United States (EPRI) indicate that there have been a considerable number of safety incidents in energy storage power stations in recent years. The relevant statistical data on safety accidents in energy storage power stations in recent years (from 2019 to 2023) are presented in Figure 1. Specifically, the most significant failure events involving BESS from 2022 are listed in Table 1. These events have disastrous consequences due to huge initial investments and severe damage.

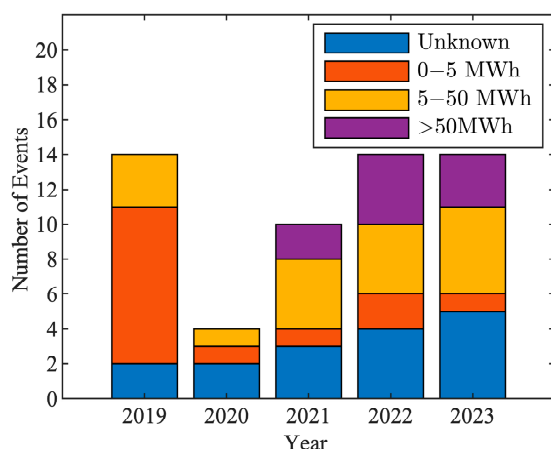


Figure 1. Safety accident statistics of BESS.

In the ninth case in Table 1, in April 2023, a battery cell in a LIB container was the source of a fire in an industrial park in the vicinity of Gothenburg, Sweden. The incident resulted in no significant injuries. The firefighters attempted to utilize a fire extinguisher to reduce the temperature of the battery; however, a subsequent explosion occurred a few minutes later. The subsequent investigation report indicated that the incident was caused by a leak within the battery cell, which resulted in a short circuit and TR.

Furthermore, in 2021, a significant fire and explosion incident involving a BESS occurred in Beijing, China, resulting in casualties among firefighters and personnel [5]. The BESS in question has a capacity of 25 MWh and uses LFP batteries. The investigation report indicates that the immediate cause of the explosion in the northern building was

an internal short-circuit failure of a single LFP battery located in the battery room of the southern building. This resulted in the battery and battery module undergoing a TR event, which subsequently led to the ignition and spread of fire. The combustion products resulting from the accident entered the energy storage room of the north building via a cable trench and subsequently dispersed, combining with air to form an explosive gas. This gas subsequently detonated upon encountering an electrical spark.

Table 1. BESS failure event in recent years.

| Number | Location | System Capacity (MWh) | Date |
|--------|---|-----------------------|---------|
| 1 | USA, CA, San Diego | 250 MWh | 2024.05 |
| 2 | Taiwan, Lanyu | 1.1 MWh | 2023.12 |
| 3 | USA, ID, Melba | 8 MWh | 2023.10 |
| 4 | Australia, Queensland, Bouldercombe | 100 MWh | 2023.09 |
| 5 | US, CA, Valley Center | 560 MWh | 2023.09 |
| 6 | France, Saucats, Barban | 98 MWh | 2023.08 |
| 7 | US, NY, Chaumont | 15 MWh | 2023.07 |
| 8 | US, NY, East Hampton | 40 MWh | 2023.05 |
| 9 | Sweden, Gothenburg, Vastra Frolunda | 0.9 MWh | 2023.04 |
| 10 | South Korea, Jeollanam-do, Yeongam-gun, Geumjeong-myeon | 251 MWh | 2022.12 |
| 11 | China, Hainan | 50 MWh | 2022.10 |
| 12 | US, CA, Moss Landing | 730 MWh | 2022.09 |
| 13 | US, AZ, Chandler | 40 MWh | 2022.04 |
| 14 | Taiwan, Taichung City, Longjing District | 1 MWh | 2022.03 |
| 15 | South Korea, Nam-gu, Ulsan | 50 MWh | 2022.01 |

The extensive deployment of BESSs and the recurrent occurrence of TR have garnered significant attention in the domain of research pertaining to the safety of BESSs. In recent years, the analysis and modeling of TR mechanisms of LIBs have constituted a significant area of focus within the broader field of battery research. A variety of models have been put forth to elucidate the underlying causes and mechanisms of TR in LIBs, offering insights from diverse perspectives. Some researchers have investigated the underlying causes and governing processes of reactions in the TR phenomenon observed in LIBs. TR is defined as an irreversible temperature rise phenomenon caused by the sum of multiple side reactions occurring at a higher rate. The phenomenon of TR is caused by the overlap and crossover of side reactions occurring simultaneously and in the same location under a multitude of abusive conditions. Once the side reactions have reached a certain level of intensity, the separator collapses and causes a short circuit in the battery, releasing a substantial amount of heat instantaneously. This initiates the TR process, which ultimately results in a significant temperature increase within the battery, leading to observable TR phenomena, such as smoking and combustion [6]. The TR reactions typically encompass the following: the decomposition of the solid electrolyte interface (SEI), the melting of the separator, the decomposition of the positive electrode material, and the decomposition and combustion of the electrolyte. In general, when the temperature reaches approximately 70–100 °C [7–10], the solid electrolyte interface separates and releases heat, resulting in a continued rise in battery temperature. Upon reaching the melting point of the separator, the solid electrolyte absorbs heat, melts, and shrinks. The separator material is typically composed of polypropylene or polyethylene. At this juncture, the characteristic temperature is approximately 120–130 °C. A notable increase in internal resistance is a

typical consequence subsequent to the melting of the separator [11]. As the side reactions persist due to the absence of separator protection between the anode and cathode, a short circuit will occur within the battery, resulting in the rapid release of a considerable amount of heat and a subsequent rise in temperature. At this juncture, the decomposition of the positive electrode material and the electrolyte may result in the release of oxygen into the battery, potentially leading to combustion and a temperature rise to 200–300 °C.

In light of the findings of the battery reaction rules analysis, some researchers have proceeded to analyze the external characteristics of TR. Liu et al. (2018) [12] proposed a model of temperature changes during the TR process of batteries. The authors classified the TR process into different stages using three characteristic temperature points: T1, T2, and T3. Other researchers conducted further analysis based on this model. The literature [13] comprehensively considers the indicators of the three stages of TR. By analyzing the relationship between T1, T3, and the total heat generation of the battery cell, it proposes a representative indicator ΔH_{TR} , which is the energy released from the cell during TR. In the paper [14], a dimensionless parameter known as the Thermal Runaway Number (TRN), is derived and experimentally validated. This parameter determines whether TR will occur in LIBs. Inspired by the TRN model, Esho et al. (2018) [15] proposed to infer the critical temperature based on the thermal balance between heat generation at different temperatures, heat conduction inside the battery, and heat dissipation outside the battery, and verified the model through experiments.

Since the 1990s, with the development of multiphysics analysis technology, extensive research has been conducted on the multiphysics and coupling of LIBs and battery packs. The multiphysics fields of LIB packs mainly include chemical fields, electric fields, thermal fields, and more. Various models have been proposed, including the Doyle–Fuller–Newman (DFN) model [16–18], the pseudo-two-dimensional (P2D) electrochemical model [19–21], the three-dimensional thermal model [22,23], the single particle model [24,25], and the equivalent circuit model [26–28]. However, these models currently involve large computational loads and require numerous parameters, making them unsuitable for practical engineering applications.

In conclusion, the majority of contemporary studies concentrate on the characterization of battery performance under static conditions, while failing to consider the intricate behaviors of batteries during charge-discharge cycles and temperature fluctuations that are commonly encountered in practical applications. Moreover, the quantification of pivotal indicators such as failure rates and TR risks, in addition to the formulation of system-level operational control strategies for BESSs, remains in its nascent stages. It is therefore imperative that further research be conducted into the safety parameters of batteries when subjected to dynamic operating conditions, that a comprehensive evaluation of the reliability of BESSs be carried out, and that the development of efficient operational control strategies be pursued in order to guarantee the safe and stable operation of these systems.

This paper identifies deficiencies in current research on TR modeling, failure rate assessment, and system optimization of batteries. It proposes a series of innovative solutions to address these shortcomings. The main contributions of this paper are as follows:

1. A simplified mathematical model is established, which accurately describes the external characteristics of the battery during thermal runaway. This provides a theoretical foundation for early warning.
2. A novel reliability assessment algorithm is devised, based on the specific structure topology and component characteristics of the energy storage system. This enables a more precise quantification of system-level thermal runaway risks.

3. An operational control algorithm for a reconfigurable battery energy storage system (RBESS) is designed with the objective of enhancing system reliability, reducing failure rates, and mitigating safety risks.

The sections are organized as follows: Section 2 describes the simplified model of the battery TR process. Section 3 introduces the operational reliability assessment algorithm of the BESS, including component reliability calculation and topology analysis. Section 4 presents and discusses the control strategy based on the RBESS, Section 5 is the case study, and Section 6 summarizes this study.

2. Materials and Methods

2.1. Battery Operating Temperature Calculation

During the charge-discharge process of a battery, heat generation can be divided into three main parts: ohmic heat (Q_o), polarization heat (Q_a), and reaction heat (Q_r). Q_r is generated from the chemical reactions that occur during the intercalation and deintercalation of Li ions, and this type of heat is reversible. Q_o is produced when the battery overcomes internal resistance during charging and discharging. Q_a arises when the electrode potential deviates from the equilibrium potential during battery operation, resulting in a voltage drop between the terminal voltage and the average open-circuit voltage. This voltage drop generates heat, known as polarization heat. The formula can be found in Appendix A.1.

A simplified model is proposed for heat generation, assuming a uniform change in the internal temperature field [29]. From this assumption, the heat generation rate (q) can be described by the following equation:

$$q = I(U - V) - IT \frac{dU}{dT} = I^2 R - IT \frac{dU}{dT} \quad (1)$$

where U is the open-circuit voltage, V is the terminal voltage, and T is the temperature. The term $I^2 R$ represents the irreversible heat, while the term $IT \frac{dU}{dT}$ represents the reversible heat.

The overall average temperature of the battery satisfies the following formula:

$$mC_p \frac{dT}{dt} = q - hA(T - T_a) \quad (2)$$

where m is the battery mass, C_p is the specific heat capacity, h is the convective heat transfer coefficient, and T_a is the ambient temperature.

2.2. TR Reaction Modeling

The TR mechanism of LIBs can be analyzed from an energy balance perspective. When the temperature of the battery reaches the threshold for initiating internal chemical reactions, the chemical components within the battery begin to decompose and release heat. If the heat generated by the battery exceeds its dissipation capacity, the internal temperature will continue to rise, further accelerating the decomposition reaction rate. During TR, the main reactions within the battery include the decomposition of the SEI layer, reactions between the anode and electrolyte, reactions between the cathode and electrolyte, melting of the separator, decomposition of the electrolyte, and decomposition of the binder.

The SEI is a thin layer that forms on the surface of the graphite negative electrode during the initial cycle. When the temperature of the battery exceeds 70 °C, the SEI will undergo decomposition, resulting in the release of heat. In the absence of the SEI, the electrolyte reacts with the graphite surface. As the temperature continues to increase, the separator begins to melt, resulting in a short circuit and the release of a substantial amount of heat. The temperature rises rapidly, leading to a convergence of diverse chemical reactions within the battery, including the decomposition of the positive electrode and the

electrolyte, as well as the combustion reaction. It is generally believed that the TR process of a battery can be divided into four stages: SEI decomposition, anode-electrolyte reaction, cathode-electrolyte reaction, and electrolyte decomposition [30].

On the other hand, considering the factors influencing TR, the state of charge (SOC) of the battery significantly affects its TR process [31]. Generally, a higher SOC leads to a lower critical temperature for TR, whereas a lower SOC usually results in an increase in the critical temperature. This also means that high SOC batteries have a lower safety margin. The Four-Equation Model for reactions involved in the TR is reported in Table 2, while Table 3 lists the relative physical and kinetic parameters used in this model.

Table 2. Four-Equation Model for TR reactions.

| TR Reactions | Reaction Rate Equation | Heat Generation Equation |
|--|--|---|
| SEI decomposition reactions | $\frac{dc_{sei}}{dt} = -A_{sei}c_{sei}^{m_{sei}} \exp\left[-\frac{E_{a,sei}}{RT}\right]$ | $Q_{sei} = -H_{sei}W_c \frac{dc_{sei}}{dt}$ |
| negative electrode-electrolyte reactions | $\frac{dc_{ne}}{dt} = -A_{ne}c_{ne}^{m_{ne,n}} \exp\left[-\frac{t_{sei}}{t_{sei0}}\right] \exp\left[-\frac{E_{a,ne}}{RT}\right]$ | $Q_{ne} = -H_{ne}W_c \frac{dc_{ne}}{dt}$ |
| positive electrode-electrolyte reactions | $\frac{d\alpha}{dt} = A_{pe}\alpha^{m_{pe,p1}}(1-\alpha)^{m_{pe,p2}} \exp\left[-\frac{E_{a,pe}}{RT}\right]$ | $Q_{pe} = -H_{pe}W_p \frac{d\alpha}{dt}$ |
| electrolyte decomposition reactions | $\frac{dc_e}{dt} = -A_e c_e^{m_e} \exp\left[-\frac{E_{a,e}}{RT}\right]$ | $Q_e = -H_e W_e \frac{dc_e}{dt}$ |

Table 3. Physical and kinetic parameters used for TR model.

| Parameters | Description | Unit |
|-------------------|---|----------|
| $A_{SEI/ne/pe/e}$ | frequency factor of the reaction | s^{-1} |
| $E_{SEI/ne/pe/e}$ | Activation energy of the reaction | J/mol |
| $c_{SEI/ne/e}$ | Dimensionless amount | - |
| α | Conversion degree of the positive electrode material. | - |
| $m_{SEI/ne/pe/e}$ | Reaction order | - |
| $H_{SEI/ne/pe/e}$ | Heat of reaction | J/kg |
| $W_{SEI/ne/pe/e}$ | Density of reactants in the medium | kg/m^3 |

2.3. The Simplified Model of the Battery TR Onset Point

In Section 2.2 of this paper, we conducted a mechanistic analysis of the side reactions during TR, enabling precise modeling of the side reaction rates and the heat generation associated with TR. However, for engineering applications, the four-step TR model requires numerous parameters and involves a complex computational process. To simplify the calculations, we performed a normalization analysis of the side reactions involved in TR. Considering that all four reaction equations during the TR process follow the Arrhenius law, we simplified the TR reaction process based on this principle and proposed a formula for calculating the onset temperature (T_{onset}) of the battery's self-heating reaction.

The simplified calculation model will employ the following mass and energy conservation equations:

$$\frac{dc}{dt} = -A c e^{-\frac{E}{RT}} \quad (3)$$

$$c_p \frac{dT}{dt} = H W A c e^{-\frac{E}{RT}} \quad (4)$$

In this study, the T_{onset} is defined as the onset point of the self-heating reaction. Given that the sensitivity of the thermal probe is $0.02 \text{ }^{\circ}\text{C}/\text{min}$, we define $\frac{dT}{dt}$ as $0.02 \text{ }^{\circ}\text{C}/\text{min}$. c_p is the heat capacity.

$$T_{\text{onset}} = \frac{-E_0}{R \ln \frac{c_p}{HAc} \frac{dT}{dt}} \quad (5)$$

where H represents the overall enthalpy change during the TR process. The total enthalpy change is given by $H = c_p \Delta T = c_p(T_3 - T_1)$ [32], making the model results independent of the choice of specific heat capacity. The temperature difference ΔT is strongly correlated with the SOC of the battery. When the SOC is high, the proportion of active materials within the battery is also high, leading to an increase in the maximum temperature reached during TR. Concurrently, the T_{onset} of TR decreases. As a result, ΔT increases as well. By expressing ΔT as a function of SOC, the formula for T_{onset} can be expressed as follows:

$$T_{\text{onset}} = \frac{-E_0}{R \ln \frac{c_p}{HAc} \frac{dT}{dt}} = \frac{-E_0}{R \ln \frac{1}{Ac \cdot \Delta T} \frac{dT}{dt}} = \frac{-E_0}{R \ln \frac{1}{Ac \cdot f(\text{SOC})} \frac{dT}{dt}} \quad (6)$$

The operating temperature of a battery is closely related to its safety. Generally, the lower the battery temperature, the safer the battery. This is because high temperatures accelerate internal chemical reactions within the battery, leading to heat accumulation and increased safety risks.

However, experience shows that during continuous discharge, the battery temperature gradually rises due to factors such as internal resistance heat generation. Simultaneously, as the SOC decreases, the remaining energy within the battery diminishes, and the T_{onset} for TR increases correspondingly. This means that the safe operating domain of the battery changes dynamically. In the context of the continuous charging process, the battery's SOC undergoes an increase, concomitant with an escalation in the battery's temperature. Concurrently, the T_{onset} of thermal runaway undergoes a decline as SOC increases. This phenomenon underscores the propensity for thermal runaway to ensue, as a consequence of battery overcharging.

In the formula presented in this paper, we observe that T_{onset} is correlated with the battery's SOC, indicating that the theoretical value of T_{onset} can be considered a dynamic safety threshold for the battery, providing valuable guidance for ensuring safe battery operation.

3. System Reliability Assessment Method

3.1. Topology of RBESS

The nominal voltage of a LIB is typically approximately 3.7 V, which is significantly lower than the voltage levels required for grid-scale energy storage. In order to satisfy the requisite voltage levels, BESs typically connect battery modules in series on the direct current (DC) side, thereby achieving a DC bus voltage of 600–800 V. Subsequently, the voltage is converted to alternating current (AC) through a power conversion system (PCS) and fed into a medium-voltage distribution network, typically at 10 kV or 35 kV. A single module typically exhibits a voltage of approximately 50 volts. In order to satisfy the system's voltage requirements, a battery cluster typically necessitates the connection of 12 to 16 modules in series.

The operation of batteries is influenced by intricate electrochemical processes, which inevitably give rise to discrepancies in the operating states of individual batteries. Furthermore, the mechanisms underlying cell degradation are intricate and diverse, and these discrepancies among batteries tend to intensify over time when they are assembled in groups. The use of traditional fixed connection methods can result in a phenomenon known as the "Short Board" effect, whereby weaker batteries are subjected to overcharging

or over-discharging, thereby accelerating their aging process in a positive feedback loop. Reconfigurable battery networks address this issue by employing power electronic switches to modify the network topology. A typical reconfigurable battery network is illustrated in Figure 2.

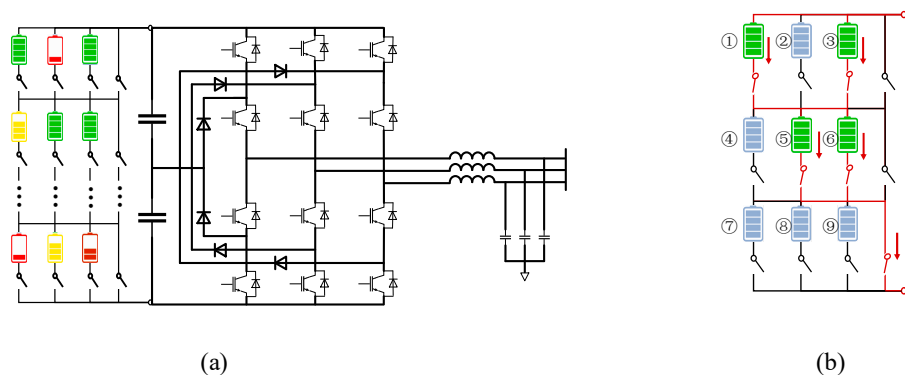


Figure 2. A typical RBESS. (a) Main structure of RBESS; (b) A typical reconfigurable battery network.

The implementation of a reconfigurable topology can effectively enhance the operational reliability of a system. During operation, the system is capable of matching the most appropriate battery module through network topology reconstruction, thereby reducing the number of times the weak link is utilized and avoiding the occurrence of the short-board effect.

As illustrated in Figure 2b, a battery network comprises nine batteries from $Bat_{(1)}$ to $Bat_{(9)}$. These batteries are arranged in three series units. The number of series units can be modified in accordance with the external voltage specifications. The system permits the bypassing or isolation of any series unit through a switch operation. While the battery can be reorganized arbitrarily within a series unit, reorganization of the battery elements in different series units is not permitted. The system selects $Bat_{(1)}$ and $Bat_{(3)}$ to form the first series unit in Figure 2b. $Bat_{(5)}$ and $Bat_{(6)}$ are chosen to form the second series unit. The third series unit is bypassed, which means that $Bat_{(7)}$, $Bat_{(8)}$, and $Bat_{(9)}$ are not working. However, the battery within different series units cannot be reorganized into new series units. Thus, for example, $Bat_{(1)}$ and $Bat_{(5)}$ cannot be connected in parallel. This paper primarily addresses the enhancement of reliability in BESSs based on this specific reconfigurable battery topology, integrating control strategies into the domain of BESS reliability analysis.

3.2. Reliability Assessment for Reconfigurable Topology

For an RBESS, it is essential to guarantee that the number of series-connected units is sufficient to maintain normal operation and satisfy the PCS voltage demands. Moreover, in the case of parallel-connected battery modules, it is of paramount importance to ensure that the number of parallel connections is at least one and that the operating current does not exceed the permissible limits. Accordingly, the RBESS is treated as a $k/n(G)$ system, and a reliability analysis is conducted.

The $k/n(G)$ system is constituted by a total of n components. The system is deemed to be functioning normally when a minimum of k of the n components are operational. Conversely, the system is deemed to be failing when the number of failed components in the system exceeds $n - k$.

If the failure probability of each component is q and the probability of normal operation is p , then it is evident that each component can be in one of two states, with $p + q = 1$. The failure probability of the $k/n(G)$ system follows a binomial distribution:

$$P_F = C_n^{k-1} p^{k-1} q^{n-k+1} + C_n^{k-2} p^{k-2} q^{n-k+2} + \dots + C_n^0 q^n \quad (7)$$

The traditional $k/n(G)$ system is predicated on the assumption that all components are identical and exhibit the same failure probability. As technological advancements and innovations in complex electromechanical products continue, and with the deepening of research into operational reliability theory, the components of a $k/n(G)$ system often find themselves at different stages of degradation and aging, resulting in varying failure rates. In order to study components of the same type but with different failure rates within a $k/n(G)$ system, this paper conducts the following analysis:

1. The system is constituted by n non-identical units, and it operates normally when at least k (where $1 \leq k \leq n$) units are functioning correctly. The system is rendered inoperable when $n - k + 1$ units have failed. At this point, the remaining $k - 1$ functioning units cease operation and no longer contribute to further failures.

2. The failure rates and repair rates of each unit remain relatively constant over a certain period. These are represented by $(\lambda_1, \lambda_2, \dots, \lambda_n)$ and $(\mu_1, \mu_2, \dots, \mu_n)$, respectively.

In a $k/n(G)$ system, the system's state space is represented by $S = \{0, 1, \dots, n - k + 1\}$, where the set of operational states is denoted by $S_{normal} = \{0, 1, \dots, n - k\}$ and the set of failure states by $S_{fault} = \{n - k + 1\}$. In a system composed of n non-identical components, if m units have failed at time t , the corresponding failure state combination is represented by C_n^m , $S_{fault,m} = S_m = \{1, 2, \dots, C_n^m\}$.

$E_m(t)$ is defined as the state at time t , where the positions of the m failed units are specified in state s , $s \in S_{fault,m}$. For example, in $m = 3$, $e = \{2, 3, 5\}$, three components have failed, and their positions are 2, 3, and 5.

After merging the states, the simplified transition relationships between the various system states are shown in Figure 3. In the diagram, λ_{s_i} and μ_{s_i} ($i = 1, 2, \dots, n - k + 1$) represent the failure rate of the transition from state S_{i-1} to S_i and the repair rate for the reverse process.

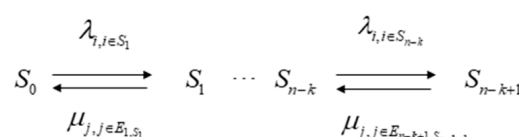


Figure 3. System state transition diagram.

Let $P_i(t)$ be the probability of event i occurring at time t . At the initial state, all components are functioning normally, and thus, $P_0(0) = 1$ and $P_1(0) = P_2(0) = \dots = P_n(0) = 0$. This can be expressed in vector form as $P(0) = [1, 0, \dots, 0]$. Similarly, let $P_i(t + \Delta t)$ denote the probability that the system is in state i at time $t + \Delta t$. According to the Chapman–Kolmogorov differential equation, we have as follows:

$$\left\{ \begin{array}{l} P_0(t + \Delta t) = P_0(t)(1 - \sum_{i \in S_1} \lambda_i \Delta t) + \sum_{i \in S_1} P_{1,i}(t) \mu_i \Delta t \\ P_{1,S_1}(t + \Delta t) = P_{1,S_1}(t) \cdot (1 - (\sum_{i \in S_1, i \notin E_{1,S_1}} \lambda_i \Delta t + \sum_{j \in E_{1,S_1}} \mu_j \Delta t)) + P_0(t) \lambda_j \Delta t + \sum_{j \in E_{2,S_2}} P_{2,j}(t) \mu_j \Delta t \\ \dots \\ P_{n-k+1,S_{n-k+1}}(t + \Delta t) = P_{n-k+1,S_{n-k+1}}(t)(1 - \sum_{\substack{i \in S_{n-k+1} \\ i \notin E_{n-k+1,S_{n-k+1}}}} \lambda_i \Delta t) + \sum_{j \in E_{n-k,S_{n-k}}} P_{n-k,j}(t) \lambda_j \Delta t \end{array} \right. \quad (8)$$

Considering that the batteries in a BESS are non-repairable components, the repair rate μ for the batteries in the BESS is $\mu = 0$. Consequently, the previous equation is modified. By rearranging and transforming the equation and letting $\Delta t \rightarrow 0$, we obtain the following expression:

$$P'(t) = P(t)Q \quad (9)$$

$$P(t) = [P_0(t), P_1(t), \dots, P_{n-k}(t), P_{n-k+1}(t)] \quad (10)$$

$$Q = \begin{pmatrix} D_0 & L_0 & & \\ O_1 & D_1 & L_1 & \\ \dots & & & \\ & O_{n-k} & D_{n-k} & L_{n-k} \\ & & O_{n-k+1} & D_{n-k+1} \end{pmatrix} \quad (11)$$

The calculation of Q can be found in Appendix A.2. System reliability and failure rate are calculated as follows:

$$R(t) = 1 - \sum_{h=1}^{C_n^{n-k+1}} P_{n-k+1,h}(t) = 1 - L^{-1}\left(\frac{1}{\Delta'}\right) \sum_{h=1}^{C_n^{n-k+1}} \sum_{i \in P_{n-k+1,S_{n-k+1}}} \lambda_i m_{n-k+1,n-k+1+h+1-i} \quad (12)$$

$$\lambda(t) = -\frac{d}{dt} \ln R(t) \quad (13)$$

3.3. Reliability Assessment for RBESS

In the RBESS shown in Figure 2a, the system is composed of batteries, MOSFETs, diodes, capacitors, IGBTs, and other devices. The operating reliability of the system depends on the reliability of the components and the topology of the system.

The failure rates of diodes, MOSFETs, and capacitors are based primarily on MIL-HDBK-217F [33].

$$\lambda_{\text{diode}} = \lambda_b \pi_T \pi_A \pi_R \pi_Q \pi_E \quad (14)$$

$$\lambda_{\text{MOSFET}} = \lambda_b \pi_T \pi_A \pi_Q \pi_E \quad (15)$$

$$\lambda_{\text{capacitor}} = \lambda_b \pi_{CV} \pi_Q \pi_E \quad (16)$$

where λ_b is the base failure rate, π_T is the temperature factor, π_A is the application factor, π_R is the power rating factor, π_Q is the quality factor, π_E is the environment factor, and π_{CV} is the capacitance factor.

The failure rate for a liquid-filled transformer λ_X is 0.468 failures/ 10^6 h [34]. The failure rate for an IGBT λ_{igbt} is 0.3000 failures/year [35].

The calculation of the battery failure rate is derived from the definition of the failure rate function. The definition of the failure rate function is as follows: the conditional probability density of a component failing per unit time after time t when the component works normally before time t . This paper assumes that the TR probability distribution of the battery follows a normal distribution with a mean of T_{onset} and a standard deviation of $\sigma = \mu/6$ [36].

$$P_{\text{tr}} \sim N(T_{\text{onset}}, \sigma) \quad (17)$$

$$\lambda(t) = \lim_{\Delta t \rightarrow 0} \frac{1}{\Delta t} P(t < T \leq t + \Delta t | T > t) \quad (18)$$

From the perspective of system structure, in the RBESS, the MOSFET switch and the battery unit (cell/module) are in series, so the overall failure rate is as follows:

$$\lambda_{\text{battery+MOSFET}} = \lambda_{\text{MOSFET}} + \lambda_{\text{battery}} \quad (19)$$

For a series unit, if it is composed of three batteries connected in parallel, the whole unit will appear as a $k/n(G)$ system or a $1/3$ system.

$$\lambda_{\text{series-unit}} = \lambda_{k/n=1/3} \quad (20)$$

For a battery pack, assuming that a pack consists of 14 series-connected cells and the redundancy is 2, then it is considered a $12/14$ system.

$$\lambda_{\text{pack}} = \lambda_{\text{series_string}} = \lambda_{k/n=12/14} \quad (21)$$

Since the DC link capacitors, transformer, and converter semiconductors are a series system in terms of reliability, the failure rate of the BESS is given by:

$$\lambda_v = \lambda_{\text{capacitor}} + \lambda_{\text{transformer}} + \lambda_{\text{converter(6_bridge_arm)}} = \lambda_c + \lambda_X + 6(\lambda_{\text{diode}} + \lambda_{\text{igbt}}) \quad (22)$$

$$\lambda_{\text{BESS}} = \lambda_v + \lambda_{\text{pack}} \quad (23)$$

4. System Operational Control Strategies for Reliability Enhancement

4.1. Weakpoint Analysis of the System

In a practical operation, the overall available capacity of a BESS is significantly influenced by the performance of its weakest battery module. In the context of a single operation of the BESS, key factors such as SOC and battery operating temperature serve as critical indicators that influence the system's performance. To comprehensively assess the system's operational reliability and prevent performance degradation due to weak battery modules, this paper proposes a criterion for identifying and evaluating weak links within the battery modules using the entropy weight method.

The entropy weight method is employed for the purpose of analyzing the weak links within the BESS. This objective weighting method assigns weights to each of the n samples (number of battery modules) across the m indicators.

Let x_{ij} represent the value of the j^{th} indicator for the i^{th} sample. As the units of measurement for each indicator differ, standardization is necessary before calculating the comprehensive indicator. This process transforms the absolute values of the indicators into relative values, addressing the issue of homogenizing heterogeneous indicators. Additionally, as the meanings of positive and negative indicators differ (with higher values being better for positive indicators and lower values being better for negative indicators), different algorithms are required to standardize the data for positive and negative indicators.

$$\begin{cases} x'_{ij}, \text{positive index} = x'_{ij} = \frac{x_{ij} - \min\{x_{1j}, \dots, x_{nj}\}}{\max\{x_{1j}, \dots, x_{nj}\} - \min\{x_{1j}, \dots, x_{nj}\}} \\ x'_{ij}, \text{negative index} = x'_{ij} = \frac{\max\{x_{1j}, \dots, x_{nj}\} - x_{ij}}{\max\{x_{1j}, \dots, x_{nj}\} - \min\{x_{1j}, \dots, x_{nj}\}} \end{cases} \quad (24)$$

1. Calculate the Proportion of the i^{th} Sample Value for the j^{th} Indicator:
Determine the proportion of the i^{th} sample value relative to the total value of the j^{th} indicator.

$$p_{ij} = \frac{x_{ij}}{\sum_{i=1}^n x_{ij}} \quad (25)$$

2. Calculate the Entropy Value for the j^{th} Indicator:

Compute the entropy value of the j^{th} indicator, reflecting the level of uncertainty or diversity within the data.

$$e_j = -k \sum_{i=1}^n p_{ij} \ln(p_{ij}), k = 1 / \ln(n) > 0 \quad (26)$$

3. Calculate the Information Entropy Redundancy:

Evaluate the redundancy or difference in information entropy for the j^{th} indicator.

$$d_j = 1 - e_j \quad (27)$$

4. Calculate the Weight of Each Indicator:

Determine the weight of each indicator based on the calculated entropy values, highlighting the relative importance of each indicator.

$$w_j = \frac{d_j}{\sum_{i=1}^m d_i} \quad (28)$$

5. Obtain the Final Comprehensive Score and Risk Index (*RI*) Rank:

Combine the weighted indicators to produce a comprehensive score for each sample.

$$RI_i = \sum_{i=1}^m w_j x'_{ij} \quad (29)$$

4.2. Operation Control Strategy

In practical operations, BESSs often incorporate appropriate redundancy in battery modules. To comply with voltage range constraints, the number of modules in series typically has a rigid redundancy, meaning there are limits on the maximum and minimum number of series-connected units. Within each series unit, redundancy in parallel connections can be set based on operational needs.

This paper adopts the reconfigurable battery network topology described earlier, with redundancy built into both series and parallel connections. The core concept of the operation strategy is “functioning within ability”. The following is the procedure for implementing the operational strategy: In conjunction with external power demand and the operating status of the battery module, the *RI* of each battery is calculated using the methodology outlined in Section 4.1. The battery modules are then matched according to the rank of *RI*, with the objective of avoiding the use of weak link batteries in the charging and discharging process. The specific strategy execution process is shown below:

1. Parameter Preparation: Gather the initial operating state set for all battery modules Ω_{SOH} , the number of series and parallel connections $N_s \times N_p$, and the network topology reconfiguration interval T_{period} . Also, obtain the redundancy status for series and parallel connections, including the minimum number of parallel branches $N_{p,min}$ (to meet current output requirements) and the minimum number of series-connected batteries per branch $N_{s,min}$ (to meet voltage output requirements).
2. Weak Link Identification: Assess the risk indicators for each battery using the algorithm described in Section 4.1.
3. Module Selection within Series Units: Rank the parallel modules within each series unit according to their risk indicators. Select the top-performing batteries to form new series units.

4. Series Unit Selection: Based on the risk indicators and the rankings from the previous step, select the top series units to form a new complete topology.
5. Charge-Discharge Simulation: Over the T_{period} , perform charge and discharge operations using the network topology selected in steps (3) and (4). Recalculate the SOC and temperature changes for the battery modules (the number of series and parallel connections will directly affect SOC and temperature variations; for instance, reducing the number of series units lowers the voltage, increases the total current, and affects the depth of charge-discharge). Assess the system's reliability under this topology using the methods from Chapter 3.
6. Move to the Next T_{period} : Repeat steps (2) to (6) until the system meets the scheduling requirements.

5. Case Study

5.1. TR Test

The selected battery for this study is a 3.2 V/20 Ah LIB provided by Tianjin Lishen. The battery features a LFP cathode and a graphite anode, with a polyethylene separator coated with ceramic. To investigate the impact of different SOC levels on the critical temperature for TR, we established various SOC charge-discharge gradients, from 0 to 100%, with each gradient being 5%.

The charging process is as follows: The test battery is installed in the testing apparatus and placed in a 25 °C testing environment. The procedure includes: resting for 10 min; a resting discharge to ensure the battery voltage drops to the cut-off voltage (set to 3 V in this experiment); constant current charging at 0.1 C until the voltage reaches 3.8 V, followed by constant voltage charging until the current decreases to 0.05 C, at which point charging stops; another 10 min rest; and finally, discharging at a constant current of 0.1 C until the battery reaches 80% capacity (80% or other levels).

In order to obtain the T_{onset} of the battery at different SOC levels, this paper uses an Accelerating Rate Calorimeter (ARC) to test the batteries charged at different levels in the text above under an adiabatic environment. ARC operates in Heat-Wait-Seek (HWS) mode. Taking the battery temperature curve at 50% SOC as an example, Figure 4 shows the temperature and temperature rise rate curve.

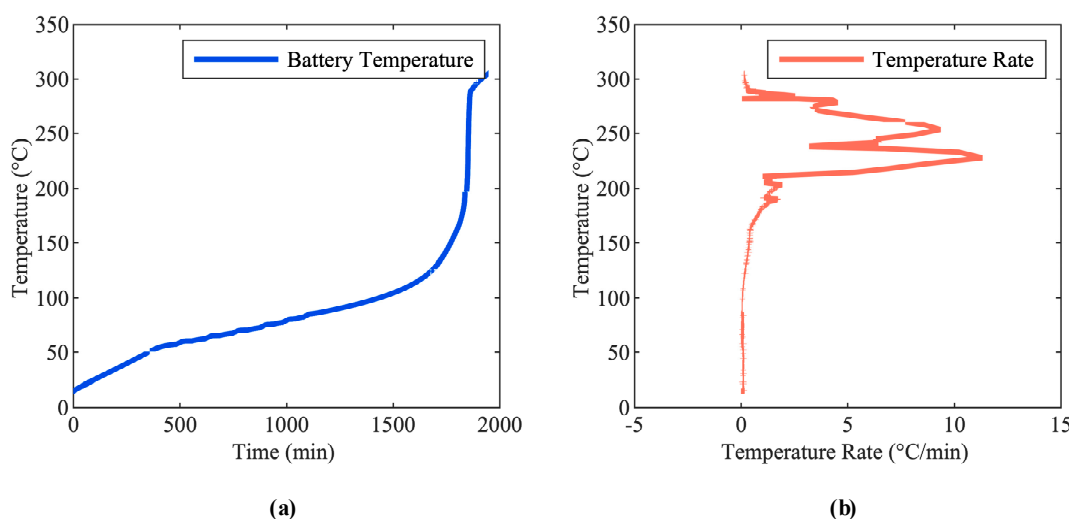


Figure 4. (a) Battery temperature curve; (b) battery temperature rise rate curve.

5.2. Experimental Results Analysis

Figure 5 shows the different stages of the TR process. In the first stage, the temperature in the incubator rises slowly, but the battery does not self-heat. In the second stage, T_1 represents the loss of thermal stability. Subsequently, the SEI decomposes and the internal heat accumulates. In the third stage, T_2 marks the triggering of TR, an internal short circuit occurs inside the battery, the temperature rise rate increases sharply, gas is generated and rapidly accumulated, and a jet flame is easily formed. T_3 is the maximum temperature that the battery can reach. Thus, the accurate identification of the onset of TR is an effective method of early warning, which can prevent the occurrence of fire accidents.

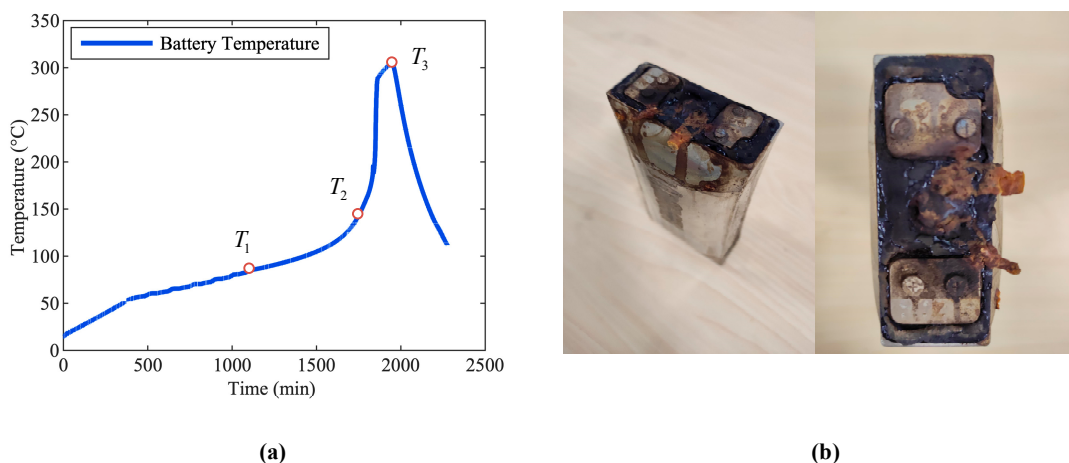


Figure 5. (a) Different stages of TR process; (b) battery sample.

As illustrated in Figure 6, the following conclusions can be drawn: As SOC increases, the T_{onset} of the self-exothermic reaction will decrease. This results in a reduction in the thermal stability and safety of the battery when the SOC is high, which also explains why the battery is susceptible to fire and explosion following overcharging. When the battery's SOC is low, its intrinsic stability is higher, as evidenced by the reduced likelihood of self-heating during the anode-to-cathode reaction. In the event of TR, batteries with low SOC typically exhibit combustion rather than fire and explosion.

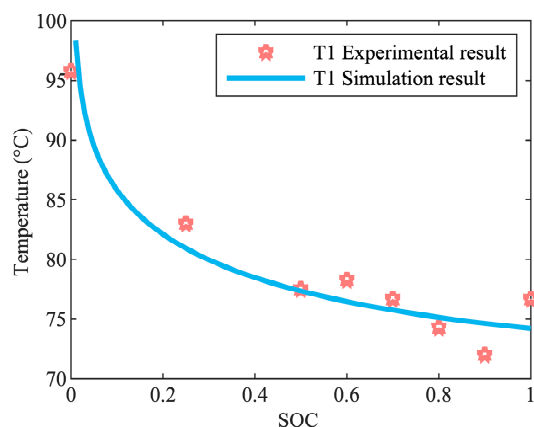


Figure 6. Comparison of experimental results and simulation results of T_{onset} .

5.3. BESS Operation Risk Analysis and Operation Optimization

The grid dispatch instructions are conducted in 15 min intervals, and there are 96 data points in a day. This section will present a simulation of the system's participation in dispatch scenarios on a 15 min timescale. The following simulation examples are based

on the BESS developed by Tsinghua University. The system utilizes the reconfigurable battery network topology shown in Figure 2a, consisting of 42 battery modules arranged in 3 parallel strings and 14 series connections. The system can operate in different configurations: 3-parallel, 3-out-of-2, or 3-out-of-1, with a minimum of 12 series connections in the series direction. The system operates for 15 min within the simulation environment, with an output current requirement of 1 C.

5.3.1. Analysis of Operating Risks and Weak Points of BESS

Assuming the BESS has a topology of 3 parallel and 14 series connections with a total of 42 battery modules, the initial capacities of the 42 battery modules range from 76% to 82%, with their internal resistance and heat exchange coefficients following a normal distribution. The system operates for 15 min, and the output current requirement is 1 C for each battery.

Figure 7 depicts the fluctuation of the operational failure rates of each battery in the system during the simulation. With regard to individual batteries, the TR failure rate is contingent upon the battery's state, which is in turn related to parameters such as SOC, temperature, heat exchange coefficient, and internal resistance. This also correlates with the battery's operational strategy, as alterations in the operational strategy influence the SOC and temperature, which in turn impact the battery's condition and the probability of TR failure.

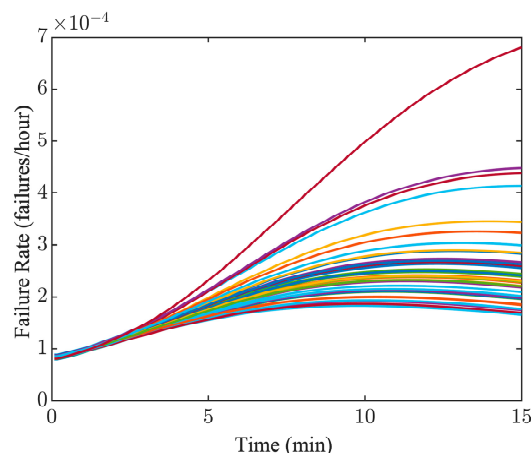


Figure 7. The failure rates of each battery.

As illustrated in Figure 7, the battery failure rate displays a fluctuating pattern, initially increasing and then declining. This pattern is observed because, during the initial phases of the discharge process, the temperature of the battery increases, thereby elevating the probability of TR. However, as the battery continues to operate, the SOC gradually decreases, and the T_{onset} of the battery's self-heating reaction rises. As the temperature differential between the battery and the self-heating reaction temperature increases, the safety margin improves, resulting in a gradual decrease in the failure rate.

When the battery management system operates in standby mode, the system-wide failure rate is zero. The failure rate of the battery management system is dependent upon the operational strategy employed by the system when the voltage varies within the permissible limits. The failure rate of power electronic components, such as IGBTs, remains relatively constant, at approximately 30 failures per 10^6 h. It can be seen that the TR failure rate of the battery in Figure 7 is much higher than that of the power electronic device. Consequently, the failure rate of the batteries themselves exerts a more pronounced influence on the overall system failure rate during the course of system operation and control.

Given the inherent variability in battery parameters, operating states, such as SOC, and temperature exhibit discrepancies across batteries operating under identical working conditions. During the dispatch task from the grid, this study employs the risk indicators proposed in Section 4.1 to identify the weak points in the BESS. Figure 8 presents the identification of six weak batteries using the *RI* proposed in this study.

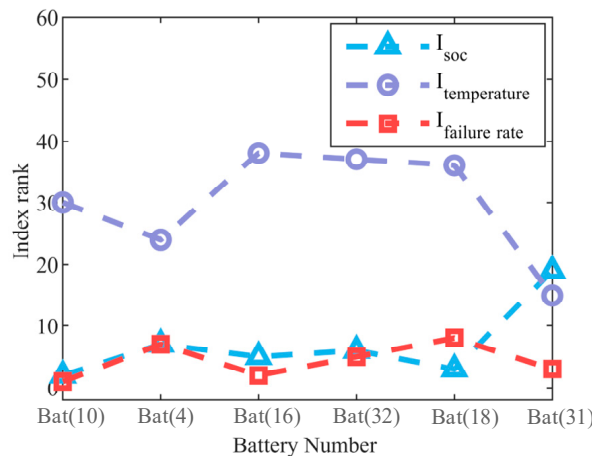


Figure 8. Weak batteries and their indexes rank.

It can be observed that, when a single indicator is used for evaluation, the ranking of weak batteries varies. To illustrate, while Battery No. 4 is ranked second in the *RI* search, it is ranked seventh for both the SOC and temperature indicators and 24th for the failure rate indicator. If evaluated exclusively based on the temperature indicator, this battery would not be identified as a potential weak point. However, from the perspectives of SOC and failure rate, this battery should be regarded as a potential cause for concern. This illustrates that the *RI* can provide a comprehensive account of the impact of both battery condition and operational state changes on system reliability, thereby facilitating a more accurate identification of weak points.

5.3.2. Optimization Effect of Control Strategy

The impact of different control strategies on the state of energy storage and system reliability is illustrated in Figure 9: (1) Under the rigid series-parallel configuration, after system operation, the variance of SOC is 0.39, the variance of temperature is 0.87, and the expected stable and safe operational time is 108.74 h. (2) By applying the *RI* indicator-based battery matching strategy proposed in this paper, after system operation, the variance of SOC is 0.048, the variance of temperature is 0.76, and the expected stable and safe operational time is 114.64 h.

(1) In the fixed topology strategy, although a larger number of battery modules participate in charging and discharging with equal depth of charge/discharge, this topology fails to mitigate the differences among battery modules during operation. Additionally, batteries with higher internal resistance tend to generate more heat, leading to significantly higher temperature extremes during operation. Over long-term use, this increases the risk of TR. Furthermore, due to the inability to isolate batteries with TR risks promptly, the system is more likely to experience overheating and high TR risks.

(2) By employing a reconfigurable battery network topology based on reliability importance indicators, the consistency of battery module capacity is better controlled during operation compared to the fixed topology strategy. Temperature control is also improved, with both variance and extreme values lower than those observed in the fixed topology strategy. As a result of better capacity and temperature control, the operational

safety of the system is significantly enhanced, with safe operational hours increased by 6%. However, due to the influence of the control strategy, temperature fluctuations in the batteries are greater than in the fixed topology strategy, which necessitates more timely control and accurate identification of weak points.

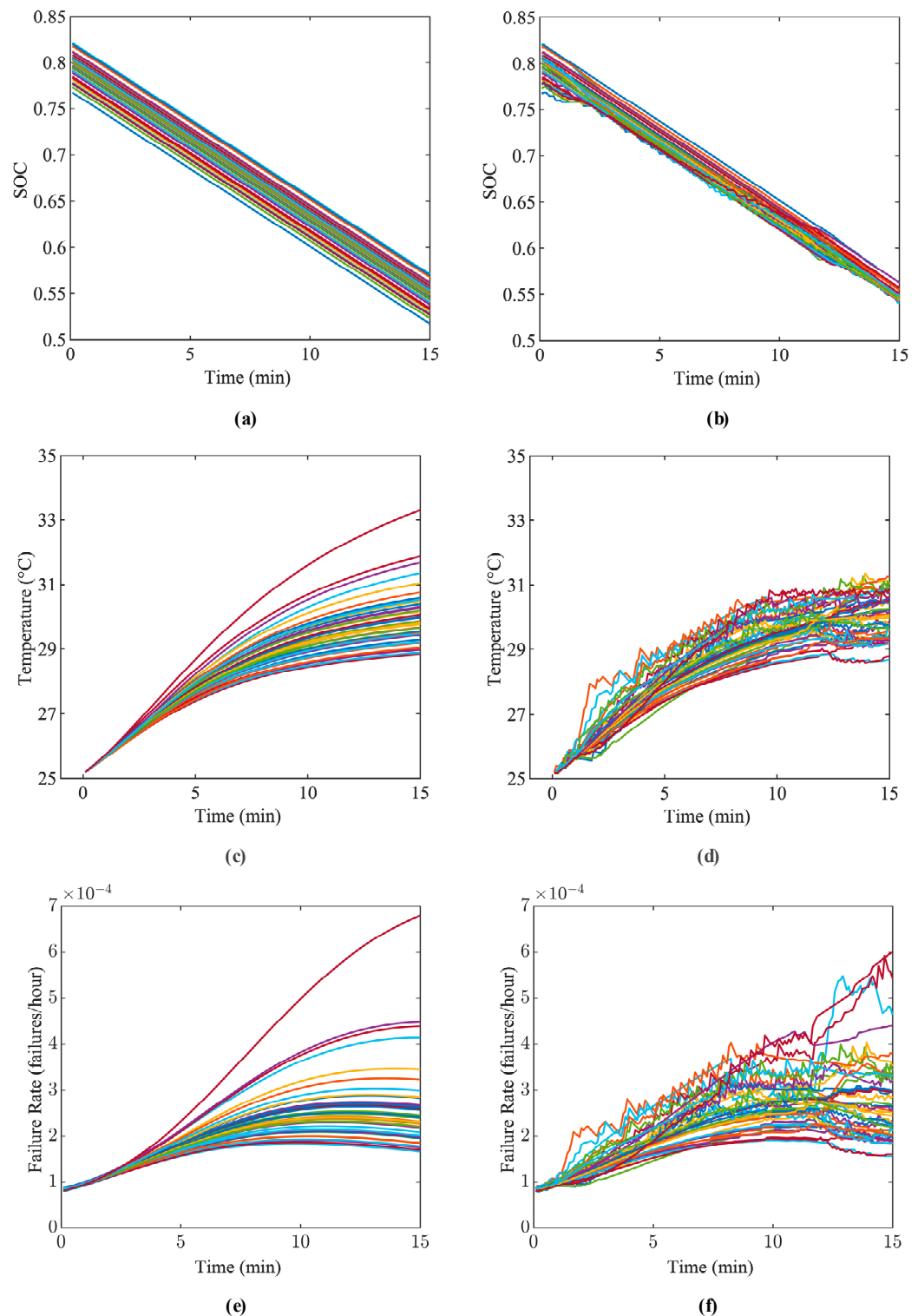


Figure 9. (a) SOC results of BESS with fixed topology; (b) SOC results of BESS with reconfigurable topology; (c) temperature results of BESS with fixed topology; (d) temperature results of BESS with reconfigurable topology; (e) failure rate results of BESS with fixed topology; (f) failure rate results of BESS with reconfigurable topology.

6. Conclusions

Battery safety has long been a major focus of research in the fields of EVs and BESSs. Reconfigurable topological designs offer precise digital scheduling and restructuring capabilities for BESSs, enabling fine-grained energy management and distribution. Faulty batteries can also be isolated promptly, preventing large-scale TR incidents.

This paper proposes a simplified modeling method for TR dynamics based on the behavior of battery TR, a reliability evaluation framework for BESSs, and a control strategy for RBESS. In this study, the T_{onset} is first introduced as a simplified calculation of the battery's operational safety boundary. By reducing the complexity of the traditional Four-Equation Model, we derive a simplified expression for T_{onset} in Equation (6). The experimental results in Figure 6 demonstrate that T_{onset} varies with the battery's operating state, decreasing as the SOC increases. This finding provides valuable guidance for managing charge and discharge operations under varying battery conditions.

Subsequently, a reliability evaluation method for the battery system is proposed. The simulation findings reveal that the failure rates of power electronic components remain relatively stable. For instance, the failure rate of IGBT devices is approximately 30 failures per 10^6 h. In contrast, as demonstrated in Figure 7, the operational failure rate of batteries can reach up to 700 failures per 10^6 h. These findings underscore the pivotal role of battery reliability in ensuring the overall reliability of the system during operation.

Finally, by analyzing battery status information, weak points in the BESS are identified, and a control strategy for RBESSs is developed. Results in Figure 9 show that RBESSs can effectively mitigate the 'Cask Effect'. The proposed control strategy improves system consistency by isolating system vulnerabilities, thereby reducing the variance in SOC and temperature among batteries after a single cycle. Furthermore, the system's peak temperature during operation is significantly reduced, enhancing safety. This study provides an effective solution for the safe and efficient use of RBESSs.

However, it should be noted that the internal parameters of the battery may be subject to alterations due to the process of aging, including capacity degradation. This, in turn, has the possibility to influence the theoretical calculation of T_{onset} . This study does not address parameter variations caused by aging, as the development of an aging degradation model falls beyond the scope of this work. Consequently, future research will concentrate on investigating the impact of aging-induced degradation on T_{onset} , accompanied by quantitative computational analysis. Furthermore, the development of rapid assessment algorithms for reliability calculations is also a key focus for future research. The efficacy and precision of reliability evaluations conducted using the Universal Generating Function (UGF) method have been demonstrated by other studies. The application of such approaches to the reliability assessment of battery components and systems has the potential to facilitate the identification of operational risks and enhance the overall safety of BESS.

Author Contributions: Conceptualization, H.X. and L.C.; methodology, H.X. and L.C.; software, H.X.; validation, H.X. and D.P.; formal analysis, H.Z.; investigation, H.X.; resources, H.X.; data curation, H.X. and L.C.; writing—original draft preparation, H.X.; writing—review and editing, H.X. and L.C.; visualization, L.C.; supervision, L.C.; project administration, H.X.; funding acquisition, L.C. All authors have read and agreed to the published version of the manuscript.

Funding: This research study was funded by the National Natural Science Foundation of China (Grant No. 52037006) and the Scientific Research Project of China Three Gorges Corporation (202203028).

Data Availability Statement: The data presented in this study are available on request from the corresponding author. The data are not publicly available due to the confidentiality of ongoing projects.

Conflicts of Interest: The authors declare no conflicts of interest.

Appendix A

Appendix A.1. Electrochemical-Thermal Model

Electrochemical-thermal coupled models offer an efficient approach for exploring the properties of LIBs. There are several models for battery simulations, such as the Newman P2D model and the single particle model (SPM). The Newman P2D model is a widely used physics-based electrochemical-thermal modeling approach among these electrochemical-thermal coupled models. The present study employs the P2D model to elucidate the mechanism of heat generation within the battery and the formula is as follows:

$$Q_o = \sigma_s^{eff} \left(\frac{\partial \phi_s}{\partial x} \right)^2 + \kappa^{eff} \left(\frac{\partial \phi_e}{\partial x} \right)^2 + \frac{2\kappa^{eff}RT}{F} (t_+ - 1) \left(1 + \frac{d \ln f \pm}{d \ln c_e} \right) \frac{\partial \ln c_e}{\partial x} \frac{\partial \phi_e}{\partial x} \quad (A1)$$

$$Q_a = J(\phi_s - \phi_e - U) \quad (A2)$$

$$Q_r = JT \frac{\partial U}{\partial T} \quad (A3)$$

where σ_s^{eff} is the effective electronic conductivity of the solid phase, κ^{eff} is the effective electronic conductivity of the liquid phase, ϕ_s is the solid phase potential, ϕ_e is the liquid phase potential, t_+ is the Li-ions transfer number, F is Faraday's constant, R is the universal gas constant, T is the temperature, $f \pm$ is the electrolyte activity coefficient, c_e is the lithium concentration in the liquid phase, J is the local current density, and U is the open-circuit potential.

Appendix A.2

The section is the calculation process of the transition probability density matrix Q . The formula is as follows:

$$Q = \begin{pmatrix} D_0 & L_0 & & & \\ O_1 & D_1 & L_1 & & \\ \cdots & & & & \\ & O_{n-k} & D_{n-k} & L_{n-k} & \\ & O_{n-k+1} & & D_{n-k+1} & \end{pmatrix} \quad (A4)$$

$$D_0 = - \sum_{i=1}^n \lambda_i \quad (A5)$$

$$L_0 = [\lambda_1, \lambda_2, \dots, \lambda_n] \quad (A6)$$

$$O_1 = [0, 0, \dots, 0]^T \quad (A7)$$

$$L_1 = \begin{pmatrix} \lambda_2 & \lambda_3 & \cdots & \lambda_n & 0 & 0 & \cdots & 0 & \cdots & \cdots & 0 \\ \lambda_1 & 0 & \cdots & 0 & \lambda_3 & \lambda_4 & \cdots & \lambda_n & \cdots & \cdots & 0 \\ 0 & \lambda_1 & \cdots & 0 & \lambda_2 & 0 & \cdots & 0 & & & \\ 0 & 0 & \cdots & 0 & 0 & \lambda_2 & \cdots & 0 & & & \\ \cdots & & & & & & & & & \lambda_n & \\ 0 & 0 & \cdots & \lambda_1 & & & & \lambda_2 & \cdots & \lambda_{n-2} & \lambda_{n-1} \end{pmatrix}_{n \times C_n^2} \quad (A8)$$

$$D_j = \left\{ diag[- \sum_{i \in S_j, i \notin P_{j,S_j}} \lambda_i] \right\}_{C_n^j} \quad (j = 1, 2, \dots, n-k) \quad (A9)$$

$$L_j = \left\{ \begin{bmatrix} \lambda_i \end{bmatrix} \right\}_{i \in P_{j,S_j}}_{C_n^j \times C_n^{j+1}} \quad (A10)$$

$$D_{n-k+1} = O_{C_n^{n-k+1} \times C_n^{n-k+1}} \quad (\text{A11})$$

References

- Wu, D.; Zhou, D.; Zhu, Q.; Wu, L. An Investigation into the Role of Residents' Cognitive Preferences in Distributed Renewable Energy Development. *Appl. Energy* **2024**, *372*, 123814. [CrossRef]
- Amir, M.; Deshmukh, R.G.; Khalid, H.M.; Said, Z.; Raza, A.; Muyeen, S.M.; Nizami, A.-S.; Elavarasan, R.M.; Saidur, R.; Sopian, K. Energy Storage Technologies: An Integrated Survey of Developments, Global Economical/Environmental Effects, Optimal Scheduling Model, and Sustainable Adaption Policies. *J. Energy Storage* **2023**, *72*, 108694. [CrossRef]
- IEA World Energy Outlook 2023—Analysis. Available online: <https://www.iea.org/reports/world-energy-outlook-2023> (accessed on 23 December 2024).
- BESS Failure Incident Database-EPRI Storage Wiki. Available online: https://storagewiki.ePRI.com/index.php/BESS_Failure_Incident_Database (accessed on 23 December 2024).
- Shen, X.; Hu, Q.; Zhang, Q.; Wang, D.; Yuan, S.; Jiang, J.; Qian, X.; Yuan, M. An Analysis of Li-Ion Induced Potential Incidents in Battery Electrical Energy Storage System by Use of Computational Fluid Dynamics Modeling and Simulations: The Beijing April 2021 Case Study. *Eng. Fail. Anal.* **2023**, *151*, 107384. [CrossRef]
- Sun, J.; Mao, B.; Wang, Q. Progress on the Research of Fire Behavior and Fire Protection of Lithium Ion Battery. *Fire Saf. J.* **2020**, *120*, 103119. [CrossRef]
- Gao, T.; Bai, J.; Ouyang, D.; Wang, Z.; Bai, W.; Mei, N.; Zhu, Y. Effect of Aging Temperature on Thermal Stability of Lithium-Ion Batteries: Part a—High-Temperature Aging. *Renew. Energy* **2023**, *203*, 592–600. [CrossRef]
- Baakes, F.; Witt, D.; Krewer, U. Impact of Electrolyte Impurities and SEI Composition on Battery Safety. *Chem. Sci.* **2023**, *14*, 13783–13798. [CrossRef]
- Maleki, H.; Deng, G.; Anani, A.; Howard, J. Thermal Stability Studies of Li-Ion Cells and Components. *J. Electrochem. Soc.* **1999**, *146*, 3224–3229. [CrossRef]
- Andersson, A.M.; Herstedt, M.; Bishop, A.G.; Edström, K. The Influence of Lithium Salt on the Interfacial Reactions Controlling the Thermal Stability of Graphite Anodes. *Electrochim. Acta* **2002**, *47*, 1885–1898. [CrossRef]
- Pastor, J.V.; García, A.; Monsalve-Serrano, J.; Golke, D. Analysis of the Aging Effects on the Thermal Runaway Characteristics of Lithium-Ion Cells through Stepwise Reactions. *Appl. Therm. Eng.* **2023**, *230*, 120685. [CrossRef]
- Liu, X.; Ren, D.; Hsu, H.; Feng, X.; Xu, G.-L.; Zhuang, M.; Gao, H.; Lu, L.; Han, X.; Chu, Z.; et al. Thermal Runaway of Lithium-Ion Batteries without Internal Short Circuit. *Joule* **2018**, *2*, 2047–2064. [CrossRef]
- Xu, C.; Wang, H.; Jiang, F.; Feng, X.; Lu, L.; Jin, C.; Zhang, F.; Huang, W.; Zhang, M.; Ouyang, M. Modelling of Thermal Runaway Propagation in Lithium-Ion Battery Pack Using Reduced-Order Model. *Energy* **2023**, *268*, 126646. [CrossRef]
- Shah, K.; Chalise, D.; Jain, A. Experimental and Theoretical Analysis of a Method to Predict Thermal Runaway in Li-Ion Cells. *J. Power Sources* **2016**, *330*, 167–174. [CrossRef]
- Esho, I.; Shah, K.; Jain, A. Measurements and Modeling to Determine the Critical Temperature for Preventing Thermal Runaway in Li-Ion Cells. *Appl. Therm. Eng.* **2018**, *145*, 287–294. [CrossRef]
- Ali, H.A.A.; Raijmakers, L.H.; Tempel, H.; Danilov, D.L.; Notten, P.H.; Eichel, R.A. A Hybrid Electrochemical Multi-Particle Model for Li-Ion Batteries. *J. Electrochem. Soc.* **2024**, *171*, 110523. [CrossRef]
- Tredenick, E.; Wheeler, S.; Drummond, R.; Sun, Y.; Duncan, S.; Grant, P. A Multilayer Doyle-Fuller-Newman Model to Optimise the Rate Performance of Bilayer Cathodes in Li Ion Batteries. *J. Electrochem. Soc.* **2024**, *171*, 060531. [CrossRef]
- Ha, S.; Onori, S. COBRAPRO: An Open-Source Software for the Doyle-Fuller-Newman Model with Co-Simulation Parameter Optimization Framework. *J. Electrochem. Soc.* **2024**, *171*, 090522. [CrossRef]
- Doyle, M.; Fuller, T.F.; Newman, J. Modeling of Galvanostatic Charge and Discharge of the Lithium/Polymer/Insertion Cell. *J. Electrochem. Soc.* **1993**, *140*, 1526–1533. [CrossRef]
- Yu, Z.; Tian, Y.; Li, B. A Simulation Study of Li-Ion Batteries Based on a Modified P2D Model. *J. Power Sources* **2024**, *618*, 234376. [CrossRef]
- Xu, J.; Sun, C.; Ni, Y.; Lyu, C.; Wu, C.; Zhang, H.; Yang, Q.; Feng, F. Fast Identification of Micro-Health Parameters for Retired Batteries Based on a Simplified P2D Model by Using Padé Approximation. *Batteries* **2023**, *9*, 64. [CrossRef]
- Li, H.; Saini, A.; Liu, C.; Yang, J.; Wang, Y.; Yang, T.; Pan, C.; Chen, L.; Jiang, H. Electrochemical and Thermal Characteristics of Prismatic Lithium-Ion Battery Based on a Three-Dimensional Electrochemical-Thermal Coupled Model. *J. Energy Storage* **2021**, *42*, 102976. [CrossRef]
- Mastali, M.; Foreman, E.; Modjtahedi, A.; Samadani, E.; Amirfazli, A.; Farhad, S.; Fraser, R.; Fowler, M. Electrochemical-Thermal Modeling and Experimental Validation of Commercial Graphite/LiFePO₄ Pouch Lithium-Ion Batteries. *Int. J. Therm. Sci.* **2018**, *129*, 218–230. [CrossRef]

24. Baba, N.; Yoshida, H.; Nagaoka, M.; Okuda, C.; Kawauchi, S. Numerical Simulation of Thermal Behavior of Lithium-Ion Secondary Batteries Using the Enhanced Single Particle Model. *J. Power Sources* **2014**, *252*, 214–228. [[CrossRef](#)]
25. Xue, C.; Jiang, B.; Zhu, J.; Wei, X.; Dai, H. An Enhanced Single-Particle Model Using a Physics-Informed Neural Network Considering Electrolyte Dynamics for Lithium-Ion Batteries. *Batteries* **2023**, *9*, 511. [[CrossRef](#)]
26. Hariharan, K.S. A Coupled Nonlinear Equivalent Circuit-Thermal Model for Lithium Ion Cells. *J. Power Sources* **2013**, *227*, 171–176. [[CrossRef](#)]
27. He, J.; Sazzad Hosen, M.; Youssef, R.; Kalogiannis, T.; Van Mierlo, J.; Berecibar, M. A Lumped Electro-Thermal Model for a Battery Module with a Novel Hybrid Cooling System. *Appl. Therm. Eng.* **2023**, *221*, 119874. [[CrossRef](#)]
28. Liu, C.; Liu, W.; Wang, L.; Hu, G.; Ma, L.; Ren, B. A New Method of Modeling and State of Charge Estimation of the Battery. *J. Power Sources* **2016**, *320*, 1–12. [[CrossRef](#)]
29. Bernardi, D. A General Energy Balance for Battery Systems. *J. Electrochem. Soc.* **1985**, *132*, 5. [[CrossRef](#)]
30. Kim, G.-H.; Pesaran, A.; Spotnitz, R. A Three-Dimensional Thermal Abuse Model for Lithium-Ion Cells. *J. Power Sources* **2007**, *170*, 476–489. [[CrossRef](#)]
31. Wang, Z.; He, T.; Bian, H.; Jiang, F.; Yang, Y. Characteristics of and Factors Influencing Thermal Runaway Propagation in Lithium-Ion Battery Packs. *J. Energy Storage* **2021**, *41*, 102956. [[CrossRef](#)]
32. Wu, H.; Chen, S.; Chen, J.; Jin, C.; Xu, C.; Rui, X.; Hsu, H.; Zheng, Y.; Feng, X. Dimensionless Normalized Concentration Based Thermal-Electric Regression Model for the Thermal Runaway of Lithium-Ion Batteries. *J. Power Sources* **2022**, *521*, 230958. [[CrossRef](#)]
33. U.S. DOD. Military Handbook MIL-HDBK-217F. In *Reliability Prediction of Electronic Equipment*; Department of Defense: Washington, DC, USA, 1991.
34. Aquilino, J.W. Report of Transformer Reliability Survey—Industrial Plants and Commercial Buildings. *IEEE Trans. Ind. Appl.* **1983**, *IA-19*, 858–866.
35. Pham, T.T.; Kuo, T.-C.; Bui, D.M. Reliability Evaluation of an Aggregate Battery Energy Storage System in Microgrids under Dynamic Operation. *Int. J. Electr. Power Energy Syst.* **2020**, *118*, 105786. [[CrossRef](#)]
36. Xia, Q.; Wang, Z.; Ren, Y.; Tao, L.; Lu, C.; Tian, J.; Hu, D.; Wang, Y.; Su, Y.; Chong, J.; et al. A Modified Reliability Model for Lithium-Ion Battery Packs Based on the Stochastic Capacity Degradation and Dynamic Response Impedance. *J. Power Sources* **2019**, *423*, 40–51. [[CrossRef](#)]

Disclaimer/Publisher’s Note: The statements, opinions and data contained in all publications are solely those of the individual author(s) and contributor(s) and not of MDPI and/or the editor(s). MDPI and/or the editor(s) disclaim responsibility for any injury to people or property resulting from any ideas, methods, instructions or products referred to in the content.